# Probing the Electronic Structures of BaTiO₃/SrTiO₃ Multilayered Film with Spatially Resolved Electron Energy-Loss Spectroscopy

Guiju Liu,[†,§] Yiqian Wang,*,[†,§] Bin Zou,[‡] Wenshuang Liang,[†] Neil M. Alford,[‡] David W. McComb,[‡] and Peter K. Petrov[‡]

[†]College of Physics & The Cultivation Base for State Key Laboratory, Qingdao University, No. 308 Ningxia Road, Qingdao 266071, People's Republic of China

[‡]Department of Materials, Imperial College London, London SW7 2AZ, United Kingdom

ABSTRACT: A multilayered film of BaTiO₃/SrTiO₃ was grown on a LaAlO₃ substrate using dual-target pulsed laser deposition technique. High-resolution scanning transmission electron microscopy observations show that the nine unit-cell BaTiO₃ layer and the three unit-cell SrTiO₃ layer are alternatively arranged in the epitaxial film where a sharp interface exists between the BaTiO₃ and SrTiO₃ layers. Electron energy-loss spectroscopy analysis demonstrates that the O-K edge spectra of SrTiO₃ and BaTiO₃ layers are quite distinct; in particular, the energy-loss peak at 547 eV in the SrTiO₃ spectrum splits into two peaks in the BaTiO₃ spectrum. The multiple-scattering calculations of O-K edge spectra for BaTiO₃ and SrTiO₃ agree well with the experimental results. The low-energy region (<542 eV) of the O-K edge spectra for both BaTiO₃ and SrTiO₃ is mainly caused by the hybridization of the O 2p with Ti 3d orbitals. The splitting peaks between 542 and 552 eV in the O-K edge spectra of BaTiO₃ are attributed to its complex crystal structure including two unequal oxygen sites and low site symmetry.
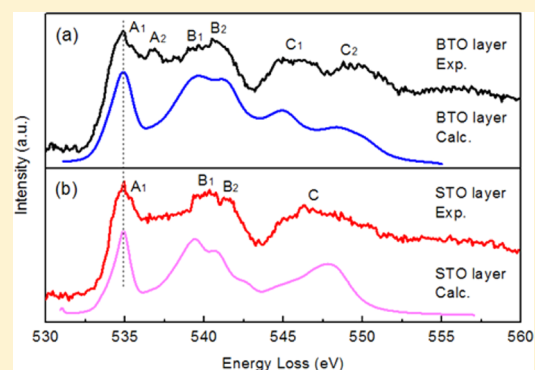
1. INTRODUCTION

Ferroelectric multilayered films have received great attention because of their unique physical properties and potential applications for various functional devices. In the past two decades, BaTiO₃/SrTiO₃ (BTO/STO) multilayered films have been considered as the most important candidates for microwave devices due to their optimized dielectric properties and enhanced polarization.[1−4] Therefore, extensive research has been devoted to obtain BTO/STO multilayered films with excellent physical properties.

It has been found that the interface and size effects affect the physical properties of the multilayered films. Especially, the enhancements of dielectric constant and voltage tunability and the decrease of the dielectric loss tangent are observed with the decrease of stacking periodicity, and are attributed to both interlayer biaxial strain effect and nanoscale effect.[5−9] Apart from the experimental studies, some theoretical investigations[10,11] revealed that the high tunabilities of multilayers result from the electrostatic and electromechanical coupling between layers, and the large dielectric response relies upon the electrostatic interactions between interlayers. In addition, the shrinking of the layer thickness down to the nanoscale produces new physical phenomena as well as challenges for characterization.

Recently, we have studied (BTO)₅/(STO)₅ multilayered films using high-resolution transmission electron microscopy (HRTEM).[12] Only threading dislocations were found in the multilayered films, while misfit dislocations, threading dis-

locations, stacking faults, and antiphase boundaries were observed in the single-layered films.[12−14] In addition to microstructure, subtle changes in atomic arrangements or distortions in the octahedra can lead to dramatic changes in the physical properties. To probe the variations in the chemical environments of oxygen atoms in STO and BTO layers, the O-K edge spectra of BTO and STO layers were acquired, and the electron energy-loss near-edge structure (ELNES) was analyzed using *ab initio* full multiple-scattering (MS) calculations.[15,16] It has been shown that features of these spectra such as peak positions and fine structures of O-K edge spectra are sensitive to the oxidation state of metal ions and crystal field splitting.[17] Also, the interpretations of the BTO spectral behaviors between 542 and 552 eV are still controversial. It is not clear whether the different spectral behaviors originate from the site symmetry or the hybridization of O 2p orbitals with higher-energy metal states. Furthermore, the simulated O-K edge spectra of BTO do not match well with the experimental results. The enhanced energy resolution in the electron energy-loss spectroscopy (EELS) measurement achieved in scanning transmission electron microscopy (STEM) equipped with monochromator provides a new opportunity to study the local chemical environments with an unprecedented resolution

for both imaging (better than 1.4 Å) and spectroscopy (0.11–0.2 eV).

In this paper, $(BTO)_9/(STO)_3$ multilayered films were epitaxially grown on (001) $LaAlO_3$ (LAO) substrates using pulsed laser deposition (PLD) technique. The interface structures and growth mechanism of multilayered films were investigated by conventional transmission electron microscopy (TEM) and HRTEM. EELS coupled with STEM was used to investigate the interface between BTO and STO layers and the differences in oxygen chemical environments. The ELNES spectra from BTO and STO layers show that there are no obvious differences in Ti-$L_{2,3}$ edges, indicating the similar coordination of Ti atoms, while there are significant changes in O-K edges, demonstrating the different oxygen chemical environments. Our results could shed light on the electronic structure and atomic coordination for BTO and STO.

2. EXPERIMENTAL SECTION

A multilayered film of BTO/STO was epitaxially grown on a 5 × 5 mm^2 LAO substrate by dual-target PLD technique (Neocera PLD system with a Lambda Physik KrF laser, λ = 248 nm), and the substrate temperature was kept at 740 °C during the deposition. Targets for the PLD system were made from ceramic powder prepared using the mixed oxide route. The film was deposited from 20-mm-diameter stoichiometric BTO and STO targets in an oxygen pressure of 300 mTorr. The energy density of the laser spot (2 × 10 mm^2) was 2.5 J/cm^2. The film thickness was measured using a Dektak-11A, and the growth rate was estimated to be 0.05 nm/pulse. Once the ablation was over, the samples were then cooled down to room temperature at a rate of 10 °C/min in an oxygen rich environment (760 Torr).

Specimens for TEM observations were prepared in a cross-sectional orientation ([010] zone-axis for the LAO substrate) using conventional techniques of mechanical polishing and ion thinning. The ion thinning was performed using a Gatan Model 691 precision ion polishing system (PIPS). The bright field (BF) imaging, selected-area electron diffraction (SAED), HRTEM, high-resolution STEM (HRSTEM), and EELS were carried out using a Titan 80-300 STEM operating at 300 kV. The EELS data are recorded in STEM mode using a spectrometer of Gatan Tridiem 865 ER with an energy resolution better than 0.2 eV and a spatial resolution of ~1.4 Å. The acquisition time for each spectrum is 20 s, and four spectra are summed together to give a better signal-to-noise ratio. The convergent and collection semiangles are 10 and 9.8 mrad, respectively.

3. RESULTS AND DISCUSSION

Figure 1a shows a schematic projection along the [010] zone-axis of BTO and STO unit cells. The structural differences between BTO and STO are (1) lattice parameters (a = 3.91 Å for STO, and a = 3.99 Å for BTO); (2) Ti atoms having a relatively large shift in the unit cells of BTO.[18] It is known that BTO and STO can form a solid solution with each other at all compositions due to their similar structures and the comparable ionic radii of Ba^{2+} and Sr^{2+}.[19] Therefore, BTO/STO multilayers or superlattices are metastable, and it is energetically favorable for these oxides to dissolve into each other forming a BSTO solid solution. However, the rate of cation interdiffusion between the Ba sites and Sr sites in these perovskites is very slow at the growth temperature used here.[20] Figure 1b is a
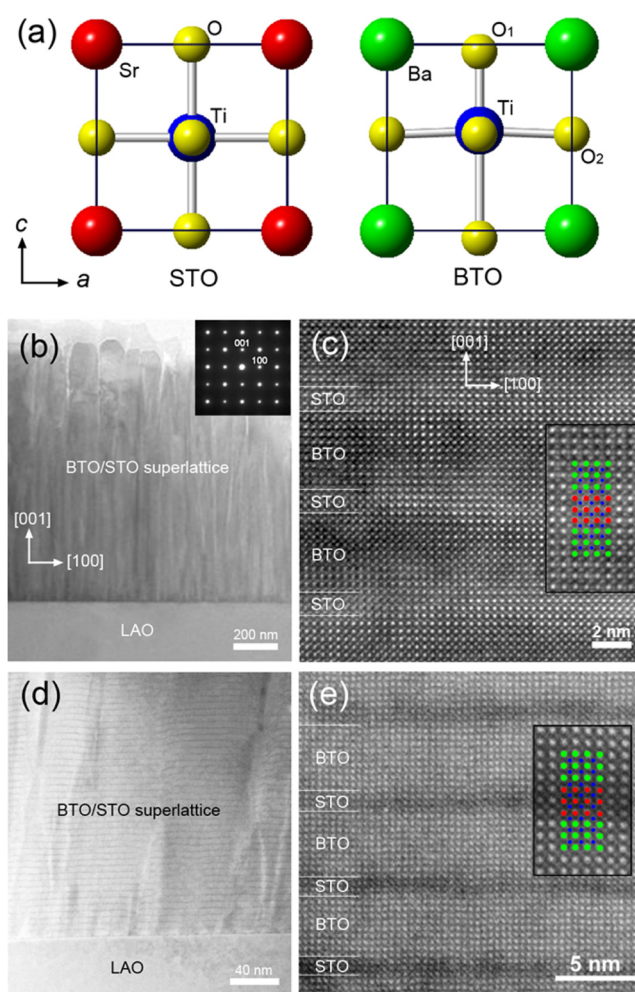

Figure 1. (a) Schematic projection along the [010] zone-axis of the BTO and STO unit cells; (b) BF TEM image and SAED pattern of the BTO/STO multilayered film on LAO substrate. (c) [010] zone-axis HRTEM image, (d) low-magnification STEM image, and (e) HRSTEM image of the BTO/STO multilayered film. Insets of parts c and e are enlarged images with the atomic model structure (green spheres, red spheres, and blue spheres represent Ba columns, Sr columns, and Ti columns, respectively).

typical BF TEM image of the BTO/STO multilayered film grown on a LAO substrate with a thickness of about 1 μm. It can be clearly seen that the interface between the substrate and the superlattice film is fairly flat and sharp, and the film exhibits a columnar structure. The columnar grain structures are produced through the epitaxial growth mechanism.[21] It is widely known that there are three major growth modes for epitaxial films, i.e., two-dimensional (2D) layer-by-layer growth mode, three-dimensional (3D) island growth mode, and a combination of 2D and 3D growth modes (2D-3D). The BTO/STO multilayered films are thought to conform to the 2D-3D growth mode. This mechanism is driven by the relaxation of elastic strain energy and consists of three steps: 2D layer-by-layer growth at the initial stage, misfit dislocation formation at the critical thickness, and 3D columnar-like growth at the final stage.[22−24] The critical thickness for Ba$_{0.75}$Sr$_{0.25}$TiO$_3$ is calculated to be about 2.22 nm using the critical thickness models,[25,26] which is thinner than the thickness of the film (1 μm); thus, misfit dislocations will form to accommodate the lattice mismatch between film and

substrate.[24] When the film is thicker than 2.22 nm, a columnar growth mode is dominant. For BTO/STO multilayers, the BTO and STO layers are alternately under compressive and tensile strain. Such strain is released at the columnar grain boundaries, and therefore, columnar structures can be produced in the film. The column diameter is about 40−50 nm, which is associated with the lattice strain between the multilayers. The alternate deposition of BTO and STO layers may cause the surface to be somewhat unstable. With the growth of the films, the unstable surface may become gradually coarsened, causing incomplete coalescence of columns. Finally, the threading dislocations form during the coalescence of columns, which is consistent with a previous report.[27] The inset is the SAED pattern taken from the superlattice region. The sharp electron diffraction spots with no splitting indicate that the BTO/STO multilayered film is well-crystallized and has a definite orientation relationship of $[010]_{STO}//[010]_{BTO}$, $\{001\}_{STO}//\{001\}_{BTO}$. The BTO and STO layers are oriented with their c-axes parallel to the growth direction.

Figure 1c shows a typical HRTEM image of the BTO/STO superlattice structure projected along the [010] direction. It clearly shows periodical alternative layers with bright and dark contrast in the film. The bright and dark contrast results from the differences of the electron scattering factor between Ba and Sr. Because Ba in the BTO layer is heavier than Sr in the STO layer, the BTO layer scatters more electrons than the STO layer, which results in the dark contrast of the BTO layer in the HRTEM images. It can be seen that the interfaces between STO and BTO are not atomically flat and sharp. Because interdiffusion of Sr and Ba is very slow at the growth temperature, we believe that the nonsharp interface is caused by the diffraction contrast, surface roughness, or intermixing of Sr and Ba during the deposition. Similar microstructure has also been observed by other groups.[28] The inset is an enlarged HRTEM image with overlaid schematics of BTO/STO, illustrating the atomic structure of the superlattice. Figure 1c indicates that lattice planes match very well although the STO/BTO interface is neither atomically abrupt nor perfectly coherent.

To study the interface of the multilayers, STEM experiments were performed due to their high space resolution and high chemical sensitivity. Figure 1d is a typical low-magnification STEM image of a BTO/STO multilayered film. It reveals the formation of a columnar structure. In the individual columns, the layered structure survives, whereas at the columnar boundaries, the layer intermixing occurs. The modulated BTO/STO superlattice structure was further confirmed by a HRSTEM image, as shown in Figure 1e. This clearly demonstrates that the BTO and STO layers have a thickness of about 3.6 and 1.2 nm, respectively. From Figure 1e, the twisted and wobbled structure can be clearly seen, and the atomic planes are not flat but show a deviation of one or two unit cells at the interface regions, indicating that the structure of the film is changed. In this imaging mode, the scattering intensity scales with the atomic number Z as $Z^{1.67}$, so that the brightest features are columns of Ba ions, the next brightest features are columns of Sr, and Ti ions are weakly visible in between.[29] The inset shows an enlarged STEM image with overlaid schematics of Ba, Sr, and Ti column positions over interface regions. These observations show that the nine unit-cell BTO layer and the three unit-cell STO layer are alternatively arranged in the film which can be indicated by $(BTO)_9/(STO)_3$.

BTO has a tetragonal structure (space group $P4mm$) with an axial ratio $c/a = 1.01$,[30] while STO has an undistorted cubic symmetry $Pm\bar{3}m$ at room temperature.[31] Since the ferroelectric properties depend on the strain in the superlattice film, the lattice parameters of STO/BTO superlattice were compared with those of bulk BTO and STO, which are summarized in Table 1. The measured in-plane lattice parameter is 3.93 Å,

Table 1. Lattice Parameters (a and c) for BTO/STO Superlattice and Bulk BTO and STO

	BTO layer	bulk BTO	STO layer	bulk STO
c (Å)	4.06	4.03	3.88	3.91
a (Å)	3.93	3.99	3.93	3.91
c/a	1.03	1.01	0.99	1.00

which is different from 3.91 Å of bulk STO and 3.99 Å of bulk BTO, but similar to the reported values in the STO/BTO superlattice with a periodicity of 2 nm.[8] The out-of-plane lattice parameters of BTO and STO superlattice layers are measured to be 4.06 and 3.88 Å from the HRTEM images, respectively, which are different from 4.03 Å of bulk BTO and 3.91 Å of bulk STO. These results indicate that the superlattice film is in an in-plane strained state compared with bulk BTO and STO, which results in an expansion of BTO and a contraction of STO along the c-axis. With the changes of lattice parameters, the crystal symmetry of STO alters from cubic to tetragonal.

In the STEM mode, we analyzed the energy resolution and performed the core level spectroscopy, atom column by atom column.[29] This approach enables us to probe internal structures directly, unlike surface-sensitive methods. Specifically, the Ti-$L_{2,3}$ edges and O-K edge spectra can be simultaneously recorded, which can be used to explore the differences of atomic chemical environments in STO layer, BTO layer, and their interface regions. Figure 2 shows the Ti-$L_{2,3}$ EELS
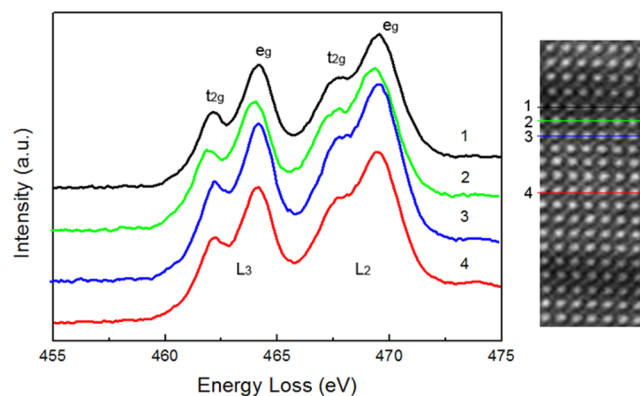

Figure 2. Ti-$L_{2,3}$ edges acquired from STO, BTO, and BTO/STO interface regions, respectively. Numbered lines in the insets show the spectra acquisition positions: 1, in the middle of the STO layer; 2 and 3, near the interface region of STO and BTO layers, respectively; 4, in the middle of the BTO layer.

spectrum acquired from STO, BTO, and their interface regions, respectively. The two peaks with lower loss energy are Ti-L_3 edges while the two peaks with higher loss energy are Ti-L_2 edges. When the Ti ion is octahedrally coordinated, the two peaks of Ti L_3 and L_2 will split into two main separate peaks.[32] As expected from the Ti^{4+} ions and their octahedral coordination, STO, BTO, and their interfaces have similar

spectra, as shown in Figure 2. The prominent four split peaks in the Ti-$L_{2,3}$ edges can be explained as excitations from $2p_{3/2}$ and $2p_{1/2}$ core electrons to unoccupied t_{2g} and e_g states. The lower energy-loss peaks of each L-edge doublet correspond to the transitions from $2p_{3/2}$ or $2p_{1/2}$ subshells to the t_{2g} states, and the higher energy-loss peaks correspond to the transitions from $2p_{3/2}$ or $2p_{1/2}$ subshells to the e_g states. The splitting between the two main peaks in both L_3 and L_2 edges is about 1.9 and 1.8 eV, respectively. Thus, no discernable difference is found between the Ti-$L_{2,3}$ edges of BTO layer, STO layer, and their interface regions. This demonstrates that there is no difference in the chemical environments of Ti ions. For the whole multilayered films, the Ti^{4+} is in octahedral coordination with oxygen, with all octahedra sharing corners.

Figure 3 shows the experimental O-K edges spectra from the BTO layer, STO layer, and the interfaces of BTO and STO
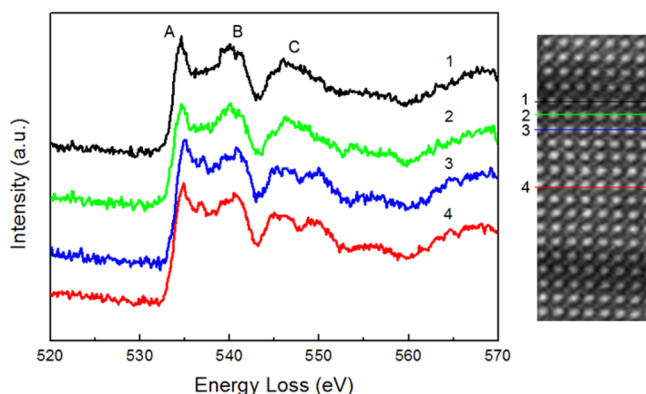

Figure 3. O-K edges acquired from STO, BTO, and BTO/STO interface regions, respectively. Numbered lines in the insets indicate the spectra acquisition positions: 1, in the middle of the STO layer; 2 and 3, near the interface region of STO and BTO layers, respectively; 4, in the middle of the BTO layer. This figure is modified from Figure 6 in ref 33.

layers. In a comparison of the O-K ELNES of the STO and BTO layers, evident differences can be identified. The most pronounced difference of the O-K edges is the splitting of peak C in the BTO layer, although slight variations exist in peak A. A previous report[34] on bulk perovskites has demonstrated that the O-K edge spectra of BTO and STO are different, and in particular the third peak of BTO splits into two peaks, which is similar to the spectra of the multilayers. This indicates that the oxygen environments of the multilayered BTO and STO layers are similar to those of the powder samples. It is worth noting that the satellite peak of peak A (energy loss of 537 eV) in the BTO layer was not observed in the bulk BTO.[15] Thus, it can be considered as a feature of multilayered BTO/STO films and their interfaces. Peak A and its satellite peak are associated with the interaction of the O atom with the Ti atom. Peak A reflects the unoccupied O 2p states hybridized with Ti 3d t_{2g} states via 2p−3d interaction. The satellite peak for BTO which occurs at the e_g band position at ~2 eV above peak A is associated with the hybridization of the O 2p states with Ti 3d e_g states. Kourkoutis et al.[35,36] obtained similar results for STO, but in our work, the e_g peak is not observed in STO. Experimental O-K edges for different oxide systems make it possible to deduce that the feature of the above two peaks is due to dispersion of the hybridized states and to the strongly distorted octahedra.[37,38] For STO, the e_g peak is completely obscured,

suggesting that the octahedral distortion is weaker than that in BTO. Remarkably, the fine features are quite similar for the O-K edge spectra acquired from the interface region and from the middle of the BTO and STO layers, respectively, suggesting that no significant interdiffusion of Ba^{2+} and Sr^{2+} takes place at interfacial regions between BTO and STO layers, which is consistent with the STEM images in Figure 1e.

To investigate the different oxygen environments in the multilayered films, we mainly focus on the O-K edge spectra of the BTO and STO layers, as shown in Figure 4a. For the O-K
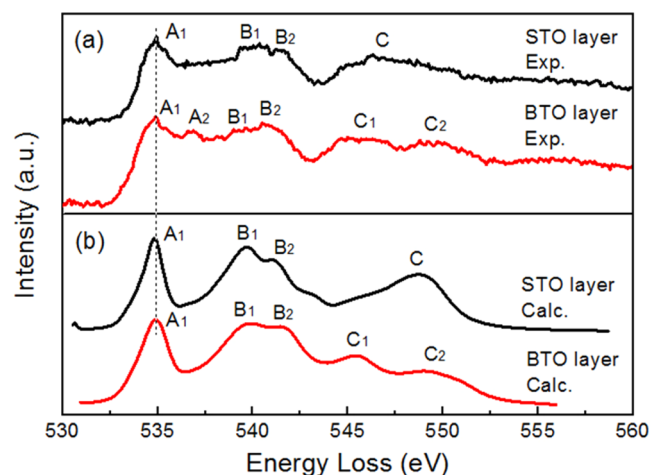

Figure 4. (a) Experimental and (b) simulated O-K edges spectra acquired from BTO and STO layers, respectively.

edges of the BTO spectrum, 6 peaks are indicated by A_1, A_2, B_1, B_2, C_1, and C_2; while for O-K edges of the STO spectrum, 4 peaks are indicated by A_1, B_1, B_2, and C. To ascertain the origin of these fine features in the ELNES spectra, the O-K edges of BTO and STO were simulated by the Wien2k program package. Tetragonal BTO with lattice parameters of $a = b = 4.0022$ Å, $c = 4.0318$ Å, and STO with lattice parameters of $a = b = 3.98$ Å, $c = 3.88$ Å, are used to calculate the ELNES spectra, and the atomic coordinates of BTO and STO are shown in Tables 2 and 3, respectively. As shown in Figure 1a, all of the

Table 2. Atomic Coordinates for BTO[a] Used for ELNES Simulation

atom	site	atomic coordinates		
		x	y	z
Ba1	1a	0	0	0
Ti1	1b	0.5	0.5	0.537
O1	1b	0.5	0.5	−0.037
O2	2c	0.5	0	0.518

[a]Tetragonal: $P4mm$, $a = b = 4.0022$ Å, $c = 4.0318$ Å, $\alpha = \beta = \gamma = 90°$.

oxygen atoms in the tetragonal STO are located at approximately equal positions (in the middle of each plane), whereas in the tetragonal BTO there are two unequal positions for oxygen atoms. The ELNES spectra of these oxygen atoms were calculated and multiplied by the corresponding number of atoms in the unit cell and then summed up. Figure 4b shows the simulated O-K edges of BTO and STO, respectively. The relative energy-loss values in the theoretical and experimental O-K edge spectra of BTO and STO are summarized in Table 4. It can be seen that the simulated O-K edges of BTO and STO

Table 3. Atomic Coordinates for STO[a] Used for ELNES Simulation

atom	site	atomic coordinates		
		x	y	z
Sr1	1a	0	0	0
Ti1	1d	0.5	0.5	0.5
O1	1c	0.5	0.5	0
O2	2e	0	0.5	0.5

[a]Tetragonal: $P4/mmm$, $a = b = 3.93$ Å, $c = 3.88$ Å, $\alpha = \beta = \gamma = 90°$.

are in good agreement with the main features of the experimental spectra. From Figure 4b, one can see that the intensity and shape of peak A_1 is well-reproduced, but peak A_2 is absent. This absence results from the multiple-scattering method used to simulate the spectrum.[16] The overlap of the peaks labeled B_1 and B_2 also makes the dispersed e_g (A_2) peak in the simulated spectrum. No obvious difference is found in peak B (539−542 eV) from both experimental and simulated O-K edges. Many researchers attributed this peak to the hybridization of the O 2p with Sr 4d and with Ba 5d states for STO[39] and BTO,[40] respectively. In our O-K ELNES, peak B splits into two peaks, labeled B_1 and B_2. Considering the difference in the out-of-plane and in-plane lattice parameters, the distance between A-site cations and oxygen atoms should be different. Thus, the splitting may be caused by the various atomic distances. Peak B_1 arises from the hybridization of the nearest O 2p with the A-site cations' d orbital, and peak B_2 results from the second-nearest O 2p hybridized with the A-site cations' d orbital, which is consistent with the report from Zhang et al.[15]

As mentioned above, both STO and BTO show tetragonal symmetry. The measured c/a ratio is 1.03 for the BTO layer, while for STO layers the c/a ratio remains very close to unity, suggesting a substantial increase of the tetragonal BTO. Moreover, the unit cell of the BTO layer is larger than that of the STO layer. The change in tetragonality and the large free space allow the ions in the unit cell to be easily polarized under an electric field. Compared with STO, the displaced Ti atoms in the BTO octahedra lead to the polarization, which breaks the symmetry of the oxygen atoms and causes the energy splitting of about 3.8 eV between C_1 and C_2 peaks. Therefore, the spectral behaviors between 542 and 552 eV in the BTO and STO are quite distinct due to the different oxygen sites and site symmetry. With the film layer changed from STO to BTO, its structure stays tetragonal, but the symmetry of the TiO_6 octahedra is decreased, and peak C in the O-K edges split into two peaks. This splitting can be well-reproduced in the ELNES simulations, as shown in Figure 4b. Sefat et al.[32] also reported similar phenomena in the $Nd_{1-x}TiO_3$ system. They found that, with x increased from 0 to 0.33, the TiO_6 coordination geometry was strongly distorted from octahedral symmetry ($m\bar{3}m$) to point symmetry (m), and the O-K edge

spectra at 540−550 eV split into two peaks. Similarly, the fine structure difference in the O-K edge can reflect the fact that BTO and STO have different crystal structures, and the oxygen in BTO and STO has distinct coordination environments. The analysis of the O-K edges therefore offers an excellent method to determine both structural and chemical environments of the BTO layer and STO layer.

4. CONCLUSIONS

In conclusion, $(BTO)_9/(STO)_3$ multilayered films were grown on LAO substrates by dual-target PLD. Sharp interfaces between nine-unit-cell BTO and three-unit-cell STO were observed. No obvious difference was found in the Ti-$L_{2,3}$ edges of BTO and STO, indicating that Ti^{4+} ions in BTO and STO layers have similar chemical environments. Experimental O-K edge spectra from the BTO layer showed a splitting of the third peak, while no splitting was observed in the spectra from the STO layer. This phenomenon was confirmed by MS calculations, suggesting a variation of the oxygen chemical environment in BTO and STO layers. The splitting of the third peak was attributed to the complex crystal structure of BTO that includes two unequal oxygen sites and low site symmetry. The enhanced energy resolution in EELS provides a unique opportunity for studying the atomic chemical environments in perovskite oxide systems.

■ AUTHOR INFORMATION

Corresponding Author
*E-mail: yqwang@qdu.edu.cn. Phone: +86 0532-8378 0318.

Author Contributions
§G.L. and Y.W. contributed to this work equally.

Notes
The authors declare no competing financial interest.

■ REFERENCES

(1) Kim, L.; Jung, D.; Kim, J.; Kim, Y. S.; Lee, J. Strain Manipulation in BaTiO3/SrTiO3 Artificial Lattice Toward High Dielectric Constant and its Nonlinearity. *Appl. Phys. Lett.* **2003**, *82*, 2118−2120.
(2) Liu, M.; Ma, C. R.; Collins, G.; Liu, J.; Chen, C. L.; Alemayehu, A. D.; Subramanyam, G.; Ding, Y.; Chen, J. H.; Dai, C.; et al. Ferroelectric BaTiO3/SrTiO3 Multilayered Thin Films for Room-Temperature Tunable Microwave Elements. *Nanoscale Res. Lett.* **2013**, *8*, 338.

Table 4. Experimental and Simulated Peak Energy-Loss Values in the O-K Edges of BTO and STO Layers, Respectively

	A		B		C	
	A_1	A_2	B_1	B_2	C_1	C_2
expt STO	534.935		539.988	541.471	547.016	
calcd STO	534.935		539.443	540.826	547.860	
expt BTO	534.935	536.817	539.443	540.633	545.779	549.642
calcd BTO	534.935		539.642	541.225	544.988	549.144

(3) Shimuta, T.; Nakagawara, O.; Makino, T.; Arai, S.; Tabata, H.; Kawai, T. Enhancement of Remanent Polarization in Epitaxial BaTiO$_3$/SrTiO$_3$ Superlattices with "Asymmetric" Structure. *J. Appl. Phys.* **2002**, *91*, 2290−2294.

(4) Tian, W.; Jiang, J. C.; Pan, X. Q.; Haeni, J. H.; Li, Y. L.; Chen, L. Q.; Schlom, D. G.; Neaton, J. B.; Rabe, K. M.; Jia, Q. X. Structural Evidence for Enhanced Polarization in a Commensurate Short-Period BaTiO$_3$/SrTiO$_3$ Superlattice. *Appl. Phys. Lett.* **2006**, *89*, 092905.

(5) Liu, M.; Ma, C. R.; Collins, G.; Liu, J.; Chen, C. L.; Dai, C.; Lin, Y.; Shui, L.; Xiang, F.; Wang, H.; et al. Interface Engineered BaTiO$_3$/SrTiO$_3$ Heterostructures with Optimized High-Frequency Dielectric Properties. *ACS Appl. Mater. Interfaces* **2012**, *4*, 5761−5765.

(6) Kim, J.; Kim, Y.; Kim, Y. S.; Lee, J.; Kim, L.; Jung, D. Large Nonlinear Dielectric Properties of Artificial BaTiO$_3$/SrTiO$_3$ Superlattices. *Appl. Phys. Lett.* **2002**, *80*, 3581−3583.

(7) Panomsuwan, G.; Takai, O.; Saito, N. Epitaxial Growth of (111)-Oriented BaTiO$_3$/SrTiO$_3$ Perovskite Superlattices on Pt(111)/Ti/Al$_2$O$_3$(0001) Substrate. *Appl. Phys. Lett.* **2013**, *103*, 112902.

(8) Tabata, H.; Tanaka, H.; Kawai, T. Formation of Artificial BaTiO$_3$/SrTiO$_3$ Superlattices using Pulsed Laser Deposition and their Dielectric Properties. *Appl. Phys. Lett.* **1994**, *65*, 1970−1972.

(9) Alford, N. Functional Films. *Mater. World* **2007**, *15*, 27−29.

(10) Zhong, S.; Alpay, S. P.; Mantese, J. V. High Dielectric Tunability in Ferroelectric-Paraelectric Bilayers and Multilayer Superlattices. *Appl. Phys. Lett.* **2006**, *88*, 132904.

(11) Okatan, M. B.; Mantese, J. V.; Alpay, S. P. Polarization Coupling in Ferroelectric Multilayers. *Phys. Rev. B: Condens. Matter Mater. Phys.* **2009**, *79*, 174113.

(12) Wang, Y. Q.; Liang, W. S.; Kong, W. J.; Petrov, P. K.; Alford, N. M. Structural Engineering of Ba$_{0.5}$Sr$_{0.5}$TiO$_3$ Epitaxial Films. *Thin Solid Films* **2012**, *520*, 5918−5921.

(13) Wang, Y. Q.; Liang, W. S.; Petrov, P. K.; Alford, N. M. Dissociation of Misfit and Threading Dislocations in Ba$_{0.75}$Sr$_{0.25}$TiO$_3$ Epitaxial Films. *Mater. Charact.* **2011**, *62*, 294−297.

(14) Wang, Y. Q.; Liang, W. S.; Petrov, P. K.; Alford, N. M. Antiphase Boundaries in Ba$_{0.75}$Sr$_{0.25}$TiO$_3$ Epitaxial Film Grown on (001) LaAlO$_3$ Substrate. *Appl. Phys. Lett.* **2011**, *98*, 091910.

(15) Zhang, J. M.; Visinoiu, A.; Heyroth, F.; Syrowatka, F.; Alexe, M.; Hesse, D.; Leipner, H. S. High-Resolution Electron Energy-Loss Spectroscopy of BaTiO$_3$/SrTiO$_3$ Multilayers. *Phys. Rev. B: Condens. Matter Mater. Phys.* **2005**, *71*, 064108.

(16) Browning, N. D.; Moltaji, H. O.; Buban, J. P. Investigation of Three-Dimensional Grain-Boundary Structures in Oxides through Multiple-Scattering Analysis of Spatially Resolved Electron-Energy-Loss Spectra. *Phys. Rev. B: Condens. Matter Mater. Phys.* **1998**, *58*, 8289−8300.

(17) deGroot, F. M. F. X-ray Absorption and Dichroism of Transition Metals and their Compounds. *J. Electron Spectrosc. Relat. Phenom.* **1994**, *67*, 529−622.

(18) Tabata, H.; Tanaka, H.; Kawai, T.; Okuyama, M. Strained SrTiO$_3$/BaTiO$_3$ Superlattices Formed by Laser Ablation Technique and their High Dielectric Properties. *Jpn. J. Appl. Phys.* **1995**, *34*, 544−547.

(19) Levin, E. M.; Robbins, C. R.; McMurdie, H. F. *Phase Diagrams for Ceramists*; Reser, M. K., Ed.; American Ceramic Society: Columbus, 1964; Vol. *1*, pp 195.

(20) Schlom, D. G.; Haeni, J. H.; Lettieri, J.; Theis, C. D.; Tian, W.; Jiang, J. C.; Pan, X. Q. Oxide Nano-Engineering Using MBE. *Mater. Sci. Eng., B* **2001**, *87*, 282−291.

(21) Jia, C. L.; Urban, K.; Hoffmann, S.; Waser, R. Microstructure of Columnar-Grained SrTiO$_3$ and BaTiO$_3$ Thin Films Prepared by Chemical Solution Deposition. *J. Mater. Res.* **1998**, *13*, 2206−2217.

(22) Jiang, J. C.; Meletis, E. I.; Gnanasekar, K. I. Self-Organized, Ordered Array of Coherent Orthogonal Column Nanostructures in Epitaxial La$_{0.8}$Sr$_{0.2}$MnO$_3$ Thin Films. *Appl. Phys. Lett.* **2002**, *80*, 4831−4833.

(23) Visinoiu, A.; Scholz, R.; Alexe, M.; Hesse, D. Morphology Dependence of the Dielectric Properties of Epitaxial BaTiO$_3$ Films and Epitaxial BaTiO$_3$/SrTiO$_3$ Multilayers. *Appl. Phys. A: Mater. Sci. Process.* **2005**, *80*, 229−235.

(24) Ding, Y.; Chen, J. H.; He, J. M.; Liu, M.; Ma, C. R.; Chen, C. L. Interface Structures and Strain Relaxation Mechanisms of Ferroelectric BaTiO$_3$/SrTiO$_3$ Multilayers on (001) MgO Substrates. *J. Cryst. Growth* **2013**, *383*, 19−24.

(25) People, R.; Bean, J. C. Calculation of Critical Thickness Versus Lattice Mismatch for Ge$_x$Si$_{1-x}$/Si Strained-Layer Heterostructures. *Appl. Phys. Lett.* **1985**, *47*, 322−324.

(26) Braun, A.; Briggs, K. M.; Böni, P. Analytical Solution to Matthews' and Blakeslee's Critical Dislocation Formation Thickness of Epitaxially Grown Thin Films. *J. Cryst. Growth* **2002**, *241*, 231−234.

(27) Misirlioglu, I. B.; Vasiliev, A. L.; Aindow, M.; Alpay, S. P.; Ramesh, R. Threading Dislocation Generation in Epitaxial (Ba,Sr)-TiO$_3$ Films Grown on (001) LaAlO$_3$ by Pulsed Laser Deposition. *Appl. Phys. Lett.* **2004**, *84*, 1742−1744.

(28) Shaw, T. M.; Gupta, A.; Chern, M. Y.; Batson, P. E.; Laibowitz, R. B.; Scott, B. A. Atomic-Scale Oxide Superlattices Grown by RHEED Controlled Pulsed-Laser Deposition. *J. Mater. Res.* **1994**, *9*, 2566−2573.

(29) Ohtomo, A.; Muller, D. A.; Grazul, J. L.; Hwang, H. Y. Artificial Charge-Modulation in Atomic-Scale Perovskite Titanate Superlattices. *Nature* **2002**, *419*, 378−380.

(30) Harada, J.; Pedersen, T.; Barnea, Z. X-ray and Neutron Diffraction Study of Tetragonal Barium Titanate. *Acta Crystallogr., Sect. A: Cryst. Phys., Diffr., Theor. Gen. Crystallogr.* **1970**, *26*, 336−344.

(31) Abramov, Y. A.; Tsirelson, V. G.; Zavodnik, V. E.; Ivanov, S. A.; Brown, I. D. The Chemical Bond and Atomic Displacements in SrTiO$_3$ from X-ray Diffraction Analysis. *Acta Crystallogr., Sect. B: Struct. Sci.* **1995**, *51*, 942−951.

(32) Sefat, A. S.; Amow, G.; Wu, M. Y.; Botton, G. A.; Greedan, J. E. High-Resolution EELS Study of the Vacancy-Doped Metal/Insulator System, Nd$_{1-x}$TiO$_3$, x = 0 to 0.33. *J. Solid State Chem.* **2005**, *178*, 1008−1016.

(33) Petrov, P. K.; Zou, B.; Wang, Y. Q.; Perkins, J. M.; McComb, D. V.; Alford, N. M. STO/BTO Modulated Superlattice Multilayer Structures with Atomically Sharp Interfaces. *Adv. Mater. Interfaces* **2014**, *1*, 1300116.

(34) Harkins, P.; McComb, D. W.; MacKenzie, M.; Craven, A. J. ELNES of Titanate Perovskites − A Probe of Structure and Bonding. *Inst. Phys. Conf. Ser.* **2004**, *179*, 119−122.

(35) Kourkoutis, L. F.; Xin, H. L.; Higuchi, T.; Hotta, Y.; Lee, J. H.; Hikita, Y.; Schlom, D. G.; Hwang, H. Y.; Muller, D. A. Atomic-Resolution Spectroscopic Imaging of Oxide Interfaces. *Philos. Mag.* **2010**, *90*, 4731−4749.

(36) Zhang, Z. L.; Sigle, W.; Rühle, M. Atomic and Electronic Characterization of the *a*[100] Dislocation Core in SrTiO$_3$. *Phys. Rev. B: Condens. Matter Mater. Phys.* **2002**, *66*, 094108.

(37) deGroot, F. M. F.; Fuggle, J. C.; Thole, B. T.; Sawatzky, G. A. *L$_{2,3}$* X-ray-Absorption Edges of *d*^{0} Compounds: K$^+$, Ca^{2+}, Sc^{3+}, and Ti^{4+} in *O$_h$* (Octahedral) Symmetry. *Phys. Rev. B: Condens. Matter Mater. Phys.* **1990**, *41*, 928−937.

(38) Brydson, R.; Sauer, H.; Engel, W.; Hofer, F. Electron Energy-Loss Near-Edge Structures at the Oxygen *K* Edges of Titanium (IV) Oxygen Compounds. *J. Phys.: Condens. Matter* **1992**, *4*, 3429−3437.

(39) Torres-Pardo, A.; Gloter, A.; Zubko, P.; Jecklin, N.; Lichtensteiger, C.; Colliex, C.; Triscone, J. M.; Stéphan, O. Spectroscopic Mapping of Local Structural Distortions in Ferroelectric PbTiO$_3$/SrTiO$_3$ Superlattices at the Unit-Cell Scale. *Phys. Rev. B: Condens. Matter Mater. Phys.* **2011**, *84*, 220102.

(40) Kurata, H.; Isojima, S.; Kawai, M.; Shimakawa, Y.; Isoda, S. Local Analysis of the Edge Dislocation Core in BaTiO$_3$ Thin Film by STEM-EELS. *J. Microsc.* **2009**, *236*, 128−131.